A Modified DQ Impedance Model of Three-Phase Grid-Connected Inverter-Grid System Considering Coupling between Inverter and Grid

Zhou, Weihua; Wang, Yanbo; E. Torres-Olguin, Raymundo; Liu, Dong; Chen, Zhe

Published in:
Proceedings of 2020 IEEE Applied Power Electronics Conference and Exposition (APEC)

DOI (link to publication from Publisher):
10.1109/APEC39645.2020.9124173

Publication date:
2020

Document Version
Accepted author manuscript, peer reviewed version

A Modified DQ Impedance Model of Three-Phase Grid-Connected Inverter-Grid System Considering Coupling between Inverter and Grid

Weihua Zhou*, Yanbo Wang*, Raymundo E. Torres-Olguin†, Dong Liu* and Zhe Chen*
*Department of Energy Technology, Aalborg University, Aalborg, Denmark
wez@et.aau.dk, ywa@et.aau.dk, dli@et.aau.dk, zch@et.aau.dk
†SINTEF Energy Research Institute, Trondheim, Norway
raymundo.torres-olguin@sintef.no

***Abstract*—This paper presents a modified dq impedance model of the three-phase voltage source grid-connected inverter (GCI)-grid system considering coupling effect between GCI part and grid part for small-signal stability analysis. Steady-state terminal voltage and current information of the GCI part which are necessary in conventional dq impedance modelling methods are calculated based on grid parameters, i.e., grid voltage and grid impedance, and current references of current-controlled GCI or power references of power-controlled GCI. In addition, effects of dynamics of grid voltage and phase-locked loop (PLL) on dq impedance characteristics of grid part are also investigated, which enables the modified dq impedance model of grid part to relate with that of GCI part. The modified dq impedance model of the GCI part which takes the effects of grid voltage and grid impedance into account need not know steady-state terminal voltage and current information. In addition, the modified dq impedance model of grid part may provide accurate stability analysis during grid voltage changes. The insight of instability mechanism of the GCI-grid coupling system may be facilitated using the modified dq impedance models. Simulation results are given to validate correctness of the proposed dq impedance model of the GCI-grid system, and effectiveness of the dq impedance model for stability analysis.**

***Index Terms*—Coupling effect, dq impedance model, grid-connected inverter, grid dynamics, stability analysis, terminal voltage.**

I. Introduction

Recently, renewable energies, such as wind power and solar power, have been increasingly penetrating into existing utility grid. Voltage source grid-connected inverters (GCIs), as important interfaces, are widely used to transmit the generated electricity into utility grid [1]. However, instability phenomena can be triggered in various frequency ranges when undesired impedance interaction between GCIs and weak grid happens [2]–[4]. Impedance-based stability analysis methods for three-phase AC systems have been proposed to investigate the oscillation mechanism [5], where the key step is to establish efficient impedance models of GCI part and grid part [6].

This work was supported by the ForskEL and EUDP project "Voltage Control and Protection for a Grid towards 100% Power Electronics and Cable Network (COPE)" (Project No.: 880063).

As for the impedance modelling of GCI part, phasor-domain, sequence-domain and dq-domain impedance models have recently been developed [3], [7]–[14]. Frequency coupling and non-linearity phenomena cannot be captured by phasor-domain impedance model [4], [7]. In addition, modelling procedure of sequence impedance model is relatively complicated [11], [12]. On the contrary, non-linearity of the GCI, e.g., power control loop and phase-locked loop (PLL), can be captured by dq impedance model, and its derivation procedure is relatively simple [3]. It's also found that the sequence-domain impedance model can be obtained by applying simple matrix transformation on the dq-domain impedance model [15]–[17]. Therefore, dq-domain impedance model is superior to the other two impedance models from the perspective of accuracy and complicity, and has been widely used for stability assessment of power electronics-dominated power systems [3], [13], [14], [18].

The dq impedance model of a GCI which consists of outer power control loop, inner current control loop and PLL is derived in [3]. It's found that the dq impedance model is influenced by operation points, e.g., duty cycle, dq axles currents and terminal voltage magnitude. At steady state, duty cycle and dq axles currents of the power-controlled GCI are dependent on terminal voltage which is usually obtained by running power flow [19]. However, only when the power system is stable, simulation results of the power flow are accurate. In addition, the procedure is time consuming [19]. On the other hand, terminal voltage of the GCI is dependent on grid parameters, i.e., grid voltage and grid impedance [20]–[23]. It means that the dq impedance model of the GCI may be represented by grid parameters, and power flow can be avoided. In addition, the grid parameters-dependent dq impedance model of the GCI may facilitate understanding and reveling the instability mechanism of GCI-grid coupling system. Recently, the sequence-domain impedance model of the GCI considering the effects of grid impedance and frequency coupling is presented in [24], which shows that the modified sequence-domain impedance is able to provide accurate stability analysis compared with the conventional impedance models which ignore the effects of grid impedance and frequency coupling. Similarly, a single-frequency output impedance model of the single-phase GCI which is derived based on the multi-frequency principle is developed in [25], which is able to capture the effects of grid impedance and frequency coupling of the PLL. However, the effects of GCI part on grid part impedance are not investigated in [24], [25].

As for impedance modelling of grid part, conventional impedance modelling method assumes that its small-signal model is not affected by GCI part and grid voltage dynamics [3]. The dq impedance model can easily be calculated by performing basic circuit series and parallel operations on grid components, i.e., grid resistance, inductance and capacitance [3]. However, in [22], it's shown that the small-signal model of grid part is affected by PLL parameters and operating point. The control model of wind power plants and transmission line electromagnetic dynamics are combined in a linear model. And system stability is assessed by the open loop transfer function of the linear system model [22]. The small-signal modelling method of grid part paves a path to establish the dq impedance model of grid part considering PLL dynamics and operating point.

In this paper, the modified dq impedance models of GCI-grid coupling system under both power control mode and current control mode are presented. As for GCI part, terminal voltage and current of the GCI are calculated based on grid parameters, i.e., grid voltage and grid impedance, and current/power references. Therefore, calculation of operating point is not needed. In addition, grid dynamics can be reflected in the modified GCI impedance model, which is able to better understand how grid parameters influence dq impedance characteristics of the GCI. As for grid part, an operation point and grid voltage-dependent dq impedance model is established, which can be more accurate than the conventional grid impedance modelling method.

The rest of this paper is organized as follows. In Section II, the small-signal model of the GCI part is established, based on which the modified dq impedance model of GCI part is derived. The small-signal model of the grid part is established, based on which the modified dq impedance model of grid part is presented in Section III. In Section IV, simulation verification is performed. Finally, conclusions are drawn in Section V.

II. Modified DQ Impedance Model of GCI Part

In this section, existing dq impedance models of the GCI part are first reviewed, followed by explanation of the modified dq impedance models.

A. Existing DQ Impedance Model of GCI Part

Fig. 1 shows the equivalent circuit model of single GCI connected with weak grid. The GCI is under vector control in dq reference frame, where d axis is aligned with the voltage vector at point of common coupling (PCC), as shown in Fig. 2(a). The control system commonly consists of outer power control loop, inner current control loop and PLL, of which

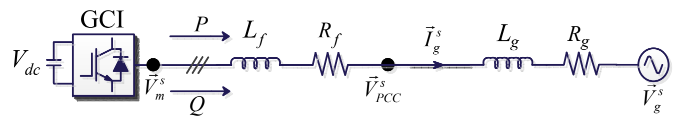

Fig. 1. Equivalent circuit model of single GCI connected with weak grid.

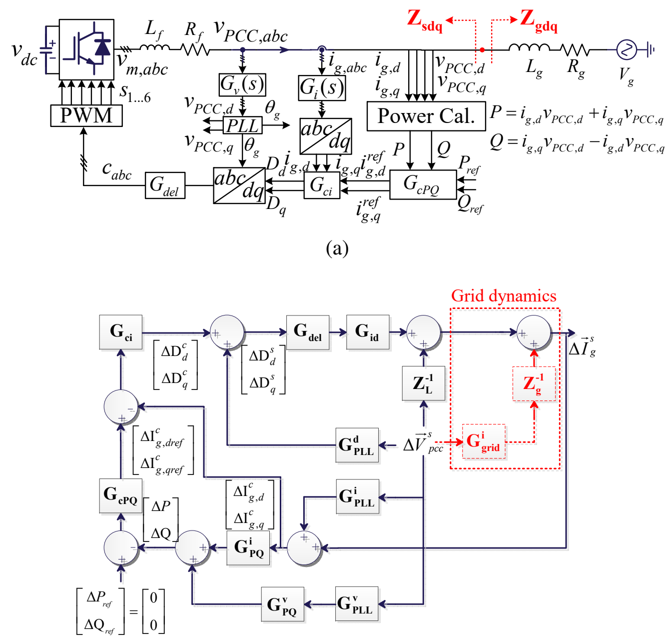

(a)

(b)

Fig. 2. (a) Control block diagram of the GCI in Fig. 1. (b) Small-signal model of the GCI-grid coupling system.

the small-signal model of the GCI part has been derived in [3], shown as the gray part in Fig. 2(b), where detailed expression of each symbol can be found in [3]. The existing dq impedance models without and with considering power control loop have also been derived in [3], shown as (1) and (2). Specifically, $\mathbf{G^v_{PLL}}$ and $\mathbf{G^i_{PQ}}$ are dependent on $\overrightarrow{V}^s_{PCC}$. $\mathbf{G^i_{PLL}}$ and $\mathbf{G^v_{PQ}}$ are dependent on $\overrightarrow{I}^s_g$. $\mathbf{G^d_{PLL}}$ is dependent on $\overrightarrow{D}^s$. It can be seen that the dq impedance models of the GCI vary with operating points $\overrightarrow{V}^s_{PCC}$, $\overrightarrow{I}^s_g$ and $\overrightarrow{D}^s$ (The superscript s indicates that the symbol is represented in the system reference frame whose d axis is aligned with voltage vector at PCC.).

B. Modified DQ Impedance Model of GCI Part

According to Fig. 1, $\overrightarrow{I}^s_g = I^s_{g,d}+jI^s_{g,q}$ and $\overrightarrow{D}^s = D^s_d+jD^s_q$ at steady state can be related by applying the Ohms's law on the filter inductance L_f and resistance R_f, shown as follows [22].

$$\frac{1}{2}V_{dc}\overrightarrow{D}^s = \overrightarrow{V}^s_m = \overrightarrow{Z}^s_f\overrightarrow{I}^s_g + \overrightarrow{V}^s_{PCC} \tag{3}$$

where $\overrightarrow{V}^s_m = V^s_{m,d}+jV^s_{m,q}$, $\overrightarrow{V}^s_{PCC} = V^s_{PCC,d}+jV^s_{PCC,q} = V_{PCC}$, $\overrightarrow{Z}^s_f = R_f + jX_f$. Fig. 3 shows the phasor diagrams of $\overrightarrow{D}^s$, $\overrightarrow{V}^s_m$, $\overrightarrow{I}^s_g$ and $\overrightarrow{V}^s_{PCC}$.

$$\mathbf{Z_{sdq\_no\_PCL}} = (\mathbf{Y_L^c} - \frac{1}{2}V_{dc}\mathbf{Y_L^g}\mathbf{G_{del}}(-\mathbf{G_{ci}}\mathbf{G_{PLL}^i} + \mathbf{G_{PLL}^d}))^{-1} \cdot (\mathbf{I} + \frac{1}{2}V_{dc}\mathbf{Y_L^g}\mathbf{G_{del}}\mathbf{G_{ci}}) \quad (1)$$

$$\begin{aligned}\mathbf{Z_{sdq\_with\_PCL}} = {} & (\mathbf{Y_L^c} - \frac{1}{2}V_{dc}\mathbf{Y_L^g}\mathbf{G_{del}}(-(\mathbf{G_{ci}}+\mathbf{G_{ci}}\mathbf{G_{cPQ}}\mathbf{G_{PQ}^i})\mathbf{G_{PLL}^i} + \mathbf{G_{PLL}^d} - \mathbf{G_{ci}}\mathbf{G_{cPQ}}\mathbf{G_{PQ}^v}\mathbf{G_{PLL}^v}))^{-1}\ldots \\ & \cdot (\mathbf{I} + \frac{1}{2}V_{dc}\mathbf{Y_L^g}\mathbf{G_{del}}(\mathbf{G_{ci}} + \mathbf{G_{ci}}\mathbf{G_{cPQ}}\mathbf{G_{PQ}^i}))\end{aligned} \quad (2)$$

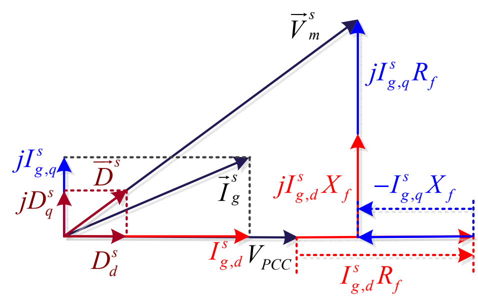

Fig. 3. Phasor diagrams of the L filter.

For the GCI under current control mode, D_d^s and D_q^s can be calculated based on (3), shown as follows.

$$\begin{aligned} D_d^s &= \frac{V_{PCC}}{0.5V_{dc}} + \frac{I_{g,d}^{ref}R_f - I_{g,q}^{ref}X_f}{0.5V_{dc}} \\ D_q^s &= \frac{I_{g,d}^{ref}X_f + I_{g,q}^{ref}R_f}{0.5V_{dc}} \end{aligned} \quad (4)$$

It can be seen from (4) that when $I_{g,d}^{ref}$ and $I_{g,q}^{ref}$ are given, D_d^s and D_q^s are only dependent on V_{PCC} and filter parameters, i.e., R_f and X_f.

For the GCI under power control mode, P_{ref} and Q_{ref} can be calculated as follows.

$$\begin{aligned} P_{ref} &= V_{PCC,d}^s I_{g,d}^s + V_{PCC,q}^s I_{g,q}^s = V_{PCC} I_{g,d}^s \\ Q_{ref} &= V_{PCC,d}^s I_{g,q}^s - V_{PCC,q}^s I_{g,d}^s = V_{PCC} I_{g,q}^s \end{aligned} \quad (5)$$

$I_{g,d}^s$ and $I_{g,q}^s$ can then be calculated as follows.

$$\begin{aligned} I_{g,d}^s &= \frac{P_{ref}}{V_{PCC}} \\ I_{g,q}^s &= \frac{Q_{ref}}{V_{PCC}} \end{aligned} \quad (6)$$

On the other hand, by substituting (6) into (4), D_d^s and D_q^s can be calculated as follows.

$$\begin{aligned} D_d^s &= \frac{V_{PCC}}{0.5V_{dc}} + \frac{P_{ref}R_f - Q_{ref}X_f}{0.5V_{dc}V_{PCC}} \\ D_q^s &= \frac{P_{ref}X_f + Q_{ref}R_f}{0.5V_{dc}V_{PCC}} \end{aligned} \quad (7)$$

By applying the Ohms' law on grid impedance R_g and L_g, voltage vector at PCC $\vec{v}_{PCC}^s$ can be calculated as follows.

$$\vec{v}_{PCC}^s = \vec{v}_g^s + \vec{Z}_g^s \vec{i}_g^s = \vec{T}_{\Delta sg}\vec{v}_g^g + \vec{Z}_f^s \vec{T}_{\Delta sc}\vec{i}_g^c \quad (8)$$

where $\vec{v}_{PCC}^s = v_{PCC,d}^s + jv_{PCC,q}^s = v_{PCC}$, $\vec{v}_g^s = v_{g,d}^s + jv_{g,q}^s$, $\vec{Z}_g^s = R_g + jX_g$, $\vec{v}_g^g = v_{g,d}^g + jv_{g,q}^g = V_g$, $\vec{T}_{\Delta sg} = \cos(\Delta sg) - j\sin(\Delta sg)$, $\vec{T}_{\Delta sc} = \cos(\Delta sc) - j\sin(\Delta sc)$. The superscripts g and c indicate that the symbols are presented in grid reference frame whose d axis is aligned with grid voltage vector and controller reference frame whose d axis is aligned with detected PCC voltage vector by PLL. The phasor diagram of grid dynamics is shown in Fig. 4.

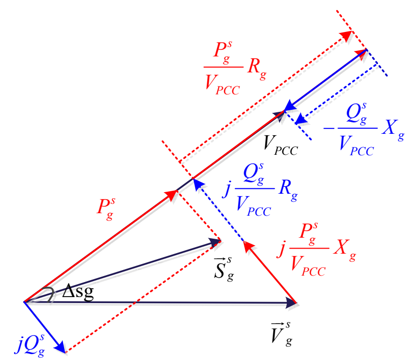

Fig. 4. Phasor diagrams of grid part.

For the GCI under current control mode, at steady state, (8) can be rewritten as follows.

$$\begin{aligned} V_{PCC,d}^s &= V_{PCC} = V_g\cos(\Delta sg) + R_g I_{g,d}^{ref} - X_g I_{g,q}^{ref} \\ V_{PCC,q}^s &= 0 = -V_g\sin(\Delta sg) + R_g I_{g,q}^{ref} + X_g I_{g,d}^{ref} \end{aligned} \quad (9)$$

Solving (9), we have

$$\begin{aligned} \Delta sg &= \cos^{-1}\frac{\sqrt{V_g^2 - (R_g I_{g,q}^{ref} + X_g I_{g,d}^{ref})^2}}{V_g} \\ V_{PCC} &= R_g I_{g,d}^{ref} - X_g I_{g,q}^{ref} + \sqrt{V_g^2 - (R_g I_{g,q}^{ref} + X_g I_{g,d}^{ref})^2} \\ 0 &= R_g I_{g,q}^{ref} + X_g I_{g,d}^{ref} - \sqrt{V_g^2 - (V_{PCC} - R_g I_{g,d}^{ref} + X_g I_{g,q}^{ref})^2} \end{aligned} \quad (10)$$

It can be seen from (4) and (10) that the two unknown parameters V_{PCC} and $\vec{D}^s$ are expressed by $\vec{I}_g^{ref}$ and grid parameters, i.e., R_g, L_g and V_g. By substituting (4) and (10) into (1), the dq impedance model of the GCI under current control mode is independent on V_{PCC} and $\vec{D}^s$, and is explicitly expressed by $\vec{I}_g^{ref}$ and grid parameters.

On the other hand, for the GCI under power control mode, at steady state, (8) can be rewritten as follows.

$$\begin{aligned} V_{PCC,d}^s &= V_{PCC} = V_g\cos(\Delta sg) + R_g\frac{P_{ref}}{V_{PCC}} - X_g\frac{Q_{ref}}{V_{PCC}} \\ V_{PCC,q}^s &= 0 = -V_g\sin(\Delta sg) + R_g\frac{Q_{ref}}{V_{PCC}} + X_g\frac{P_{ref}}{V_{PCC}} \end{aligned} \quad (11)$$

It can be derived from (11) that

$$V_{PCC}^4 + (2X_gQ_{ref} - 2R_gP_{ref} - V_g^2)V_{PCC}^2 \cdots + (R_g^2 + X_g^2)(P_{ref}^2 + Q_{ref}^2) = 0 \quad (12)$$

Solving (12), V_{PCC} can be expressed by P_{ref}, Q_{ref} and grid parameters, shown as (13) at the top of the next page. It can be seen from (6), (7) and (12) that the unknown three parameters V_{PCC}, $\overrightarrow{I}_g^s$ and $\overrightarrow{D}^s$ are expressed by P_{ref}, Q_{ref} and grid parameters. By substituting (6), (7) and (12) into (2), the dq impedance model of the GCI under power control mode is independent on V_{PCC}, $\overrightarrow{I}_g^s$ and $\overrightarrow{D}^s$, and is explicitly expressed by P_{ref}, Q_{ref} and grid parameters.

III. Modified DQ Impedance Model of Grid Part

In this section, the small-signal models of grid part under different simplifications are first established, based on which its different dq impedance models are derived.

A. Dynamics of Grid Voltage and PLL Ignored

In this case, $\vec{v}_g^s = \overrightarrow{0}$ and $\overrightarrow{T}_{\Delta sc} = 1$. (8) can be rewritten as follows.

$$\vec{v}_{PCC}^s = \overrightarrow{Z}_g^s \vec{i}_g^s \quad (14)$$

(14) can then be linearized as follows.

$$\begin{aligned} \Delta v_{PCC,d1}^s &= R_g \Delta i_{g,d}^s - X_g \Delta i_{g,q}^s \\ \Delta v_{PCC,q1}^s &= R_g \Delta i_{g,q}^s + X_g \Delta i_{g,d}^s \end{aligned} \quad (15)$$

(15) can be represented in matrix form, shown as follows.

$$\begin{bmatrix} \Delta i_{g,d}^s \\ \Delta i_{g,q}^s \end{bmatrix} = \mathbf{Z_g}^{-1} \begin{bmatrix} \Delta v_{PCC,d1}^s \\ \Delta v_{PCC,q1}^s \end{bmatrix} \quad (16)$$

where

$$\mathbf{Z_g} = \begin{bmatrix} R_g + sL_g & -X_g \\ X_g & R_g + sL_g \end{bmatrix} \quad (17)$$

It can be seen from (16) that the small signal relationship between terminal voltage and terminal current of grid part is only dependent on grid impedance.

B. Grid Voltage Dynamics Considered, and PLL Dynamics Ignored

In this case, $\vec{v}_g^s \neq \overrightarrow{0}$ and $\overrightarrow{T}_{\Delta sc} = 1$. For the GCI under current control mode, (8) can be rewritten as (18).

$$\begin{aligned} v_{PCC,d}^s &= V_g \cos(\Delta sg) + R_g i_{g,d}^s + L_g \frac{di_{g,d}^s}{dt} - \omega_1 L_g i_{g,q}^s \\ v_{PCC,q}^s &= -V_g \sin(\Delta sg) + \omega_1 L_g i_{g,d}^s + R_g i_{g,q}^s + L_g \frac{di_{g,q}^s}{dt} \end{aligned} \quad (18)$$

The steady-state solution of (18) is shown as (10) which can be perturbed and linearized as follows.

$$\begin{aligned} \Delta v_{PCC,d2}^s &= R_g \Delta i_{g,d}^s - X_g \Delta i_{g,q}^s - \frac{(X_g \Delta i_{g,d}^s + R_g \Delta i_{g,q}^s)}{A} \\ \Delta v_{PCC,q2}^s &= R_g \Delta i_{g,q}^s + X_g \Delta i_{g,d}^s + \frac{X_g \Delta i_{g,q}^s - R_g \Delta i_{g,d}^s}{B} \end{aligned} \quad (19)$$

where

$$\begin{aligned} A &= \sqrt{\left(\frac{V_g}{X_g i_{g,d}^s + R_g i_{g,q}^s}\right)^2 - 1} \\ B &= \sqrt{\left(\frac{V_g}{V_{PCC} - R_g i_{g,d}^s + X_g i_{g,q}^s}\right)^2 - 1} \end{aligned} \quad (20)$$

By comparing (15) and (19), it can be seen that when grid voltage dynamic is further considered, additional one component is added to $\Delta v_{PCC,d}^s$ and $\Delta v_{PCC,q}^s$, respectively. Note that when $V_g = 0$, (15) and (19) can be related by

$$\begin{aligned} \Delta v_{PCC,d2}^s &= \Delta v_{PCC,d1}^s + j\Delta v_{PCC,q1}^s \\ \Delta v_{PCC,q2}^s &= \Delta v_{PCC,q1}^s + j\Delta v_{PCC,d1}^s \end{aligned} \quad (21)$$

i.e.,

$$\begin{bmatrix} \Delta v_{PCC,d2}^s \\ \Delta v_{PCC,q2}^s \end{bmatrix} = \begin{bmatrix} 1 & j \\ j & 1 \end{bmatrix} \begin{bmatrix} \Delta v_{PCC,d1}^s \\ \Delta v_{PCC,q1}^s \end{bmatrix} \quad (22)$$

(19) can be represented in matrix form, shown as follows.

$$\begin{bmatrix} \Delta v_{PCC,d2}^s \\ \Delta v_{PCC,q2}^s \end{bmatrix} = \begin{bmatrix} 1 & -\frac{1}{A} \\ -\frac{1}{B} & 1 \end{bmatrix} \mathbf{Z_g} \begin{bmatrix} \Delta i_{g,d}^s \\ \Delta i_{g,q}^s \end{bmatrix} \quad (23)$$

Then, (23) can be rewritten as follows.

$$\begin{bmatrix} \Delta i_{g,d}^s \\ \Delta i_{g,q}^s \end{bmatrix} = \mathbf{Z_g^{-1} G_{grid}^i} \begin{bmatrix} \Delta v_{PCC,d2}^s \\ \Delta v_{PCC,q2}^s \end{bmatrix} \quad (24)$$

where $\mathbf{G_{grid}^i}$ is defined as follows.

$$\mathbf{G_{grid}^i} = \frac{1}{AB - 1} \begin{bmatrix} AB & B \\ A & AB \end{bmatrix} \quad (25)$$

It can be seen from (16) and (24) that additional transfer function matrix $\mathbf{G_{grid}^i}$ is added when grid voltage dynamic is further considered. Therefore, $\mathbf{G_{grid}^i}$ can depict the effect of grid voltage dynamics on small-signal relationship between $\Delta\vec{v}_{PCC}^s$ and $\Delta\vec{i}_g^s$. Note that the dq impedance model of the grid part is not symmetrical anymore when further considering grid voltage dynamics (A 2×2 matrix is symmetrical if the two diagonal components are the same, and the two off-diagonal components are opposite.).

The small-signal model of grid part in Fig. 1 can then be established, as shown in the red dotted box in Fig. 2(b).

C. Dynamics of Grid Voltage and PLL Considered

In this case, $v_g^s \neq \overrightarrow{0}$ and $\overrightarrow{T}_{\Delta sc} \neq 1$. In addition, all parameters are represented in grid reference frame. (8) is rewritten as follows.

$$\vec{v}_{PCC}^g = \vec{v}_{PCC}^s e^{j\Delta gs} = V_g + (R_g + jX_g)(i_{g,d}^c + ji_{g,q}^c)e^{j\Delta gc} \quad (26)$$

Except V_g and X_g, all other components in (26) are regarded as variables. Therefore, (26) can be linearized as follows.

$$\Delta v_{PCC,d3}^s + j\Delta v_{PCC,q3}^s + jv_{PCC,d3}^s \Delta^2 gs = e^{j\Delta sc}(R_g + jX_g)(\Delta i_{g,d}^c + j\Delta i_{g,q}^c + j(i_{g,d}^c + ji_{g,q}^c)\Delta^2 gc) \quad (27)$$

$$V_{PCC}=\sqrt{R_gP_{ref}-X_gQ_{ref}-\frac{\sqrt{V_g^4+4(R_gP_{ref}-X_gQ_{ref})V_g^2-4(X_gP_{ref}+Q_{ref}R_g)^2}}{2}+\frac{V_g^2}{2}} \tag{13}$$

Δsc can be ignored. By comparing the real parts and imaginary parts of both sides of (27), $\Delta v^s_{PCC,d3}$ and $\Delta v^s_{PCC,q3}$ can be obtained as follows.

$$\begin{aligned}\Delta v^s_{PCC,d3}&=R_g\Delta i^c_{g,d}-X_g\Delta i^c_{g,q}-(R_gi^c_{g,q}+X_gi^c_{g,d})\Delta^2gc\\ \Delta v^s_{PCC,q3}&=R_g\Delta i^c_{g,q}+X_g\Delta i^c_{g,d}+(R_gi^c_{g,d}-X_gi^c_{g,q})\Delta^2gc\\ &-V_{PCC}\Delta^2gs\end{aligned} \tag{28}$$

On the other hand, Δ^2gc can be represented as follows [22].

$$\Delta^2gc=\frac{G_{PLL}(X_g\Delta i^c_{g,d}+R_g\Delta i^c_{g,q})}{V_{PCC}+(X_gi^c_{g,q}-R_gi^c_{g,d})G_{PLL}} \tag{29}$$

where

$$G_{PLL}=\frac{K_{pPLL}s+K_{iPLL}}{s^2+K_{pPLL}s+K_{iPLL}} \tag{30}$$

where K_{pPLL} and K_{iPLL} are the proportional and integral coefficients of the PLL controller. G_{PLL} is actually the transfer function from Δ^2gs to Δ^2gc [22], i.e.,

$$\Delta^2gs=\frac{\Delta^2gc}{G_{PLL}} \tag{31}$$

Then, it can be seen from (19) and (28) that by ignoring PLL dynamics, i.e., $G_{PLL}=1$ and $\Delta\vec{i}^s_g=\Delta\vec{i}^c_g$, $\Delta v^s_{PCC,d2}$ is the same as $\Delta v^s_{PCC,d3}$. Similar with (24), (28) can also be expressed in matrix form by substituting (29) and (31) into (28).

To further illustrate the coupling relationship between the GCI part and the grid part, coupling paths are shown in Fig. 5(a). The current or power generated by the GCI part enforces the terminal voltage to change due to the dynamics of the grid part. The changed terminal voltage further influences the dq impedance characteristics of the GCI part via PLL or power control loop. On the other hand, as shown in Section III-C, the dq impedance model of the grid part is affected by terminal voltage variation due to the PLL and grid voltage characteristics.

Based on the established small-signal model of the whole system in Fig. 2, system impedance model in dq-domain can be established, as shown in Fig. 5(b), where $\mathbf{Z_{s\_modi}}(V_g,R_g,L_g)$ indicates that the dq impedance model of the GCI part is dependent on grid parameters. $\mathbf{Z_{g\_modi}}(V_g)$ indicates that the dq impedance model of the grid part is dependent on grid voltage V_g.

IV. Simulation Verification

In this section, the correctness of the established dq impedance models of GCI part and grid part is verified by simulation results in Matlab/Simulink. Furthermore, the effectiveness of the established dq impedance models for stability analysis is also shown.

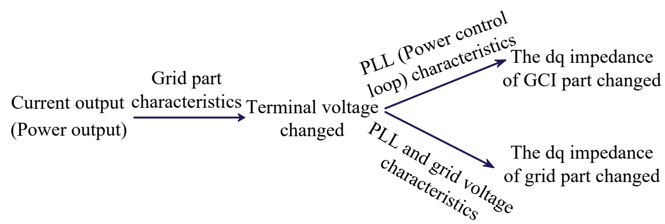

(a)

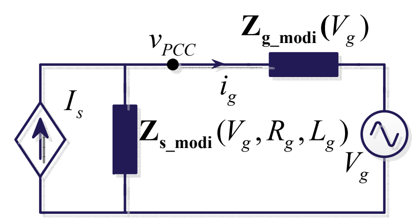

(b)

Fig. 5. (a) Coupling path between the GCI part and grid part. (b) Established dq impedance model of the GCI-grid system in Fig. 1.

A. Verification of Correctness of the Modified DQ Impedance Model of GCI Part

1) Impacts of X_g, $I^{ref}_{g,d}(P_{ref})$, $I^{ref}_{g,q}(Q_{ref})$ on V_{PCC}: Table I shows the circuit and controller parameters of the GCI in Fig. 2(a). To simplify the verification procedure, only the GCI under current control mode is considered here, whereas the theoretical analysis of the GCI under power control mode can also be performed in a similar way.

TABLE I
CIRCUIT AND CONTROLLER PARAMETERS OF THE GCI IN FIG. 1

Parameter	Value
DC-link voltage V_{dc}	1150 V
Grid fundamental frequency f_1	50 Hz
Filter inductance L_f	263 μH
Filter resistance R_f	0
Switching frequency f_{swit}	2.5 kHz
Sampling frequency f_{samp}	2.5 kHz
Grid Vrms (phase-to-phase) V_g	575 V
Proportional gain of power controller k_{pPQ}	0.0000549
Integral gain of power controller k_{iPQ}	0.03294
Proportional gain of current controller k_{pi}	0.000549
Integral gain of current controller k_{ii}	0.3294
Proportional gain of PLL K_{pPLL}	8
Integral gain of PLL K_{iPLL}	32

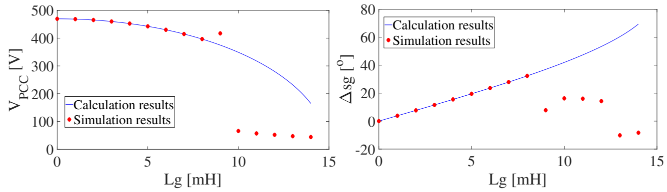

(a) (b)

Fig. 6. Impacts of X_g on V_{PCC} and Δsg. (a) Impact of X_g on V_{PCC}. (b) Impact of X_g on Δsg.

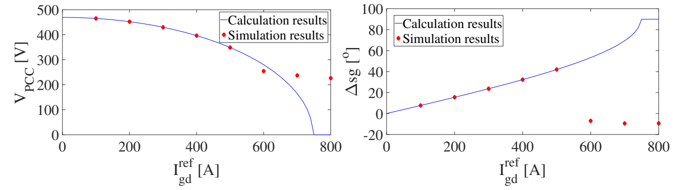

(a) (b)

Fig. 7. Impacts of $I_{g,d}^{ref}$ on V_{PCC} and Δsg. (a) Impact of $I_{g,d}^{ref}$ on V_{PCC}. (b) Impact of $I_{g,d}^{ref}$ on Δsg.

Fig. 6 shows the simulation results of V_{PCC} and Δsg with L_g varying from 0 to 14 mH with step size 1 mH, i.e., $X_g = \omega_1 L_g$ varies from 0 to 4.396 Ω, when $R_g = 0$, $I_{g,d}^{ref} = 100$ A and $I_{g,q}^{ref} = 0$. In addition, the theoretical V_{PCC} and Δsg can be calculated by (10), i.e., $V_{PCC} = \sqrt{V_g^2 - (X_g I_{g,d}^{ref})^2} = \sqrt{469.49^2 - (31400 L_g)^2}$ and $\Delta sg = \cos^{-1} \frac{\sqrt{469.49^2 - (31400 L_g)^2}}{469.49}$, which are also plotted in Figs. 6(a), (b). It can be seen that the simulation results highly agree with the theoretical analysis results when L_g is smaller than 9 mH, which validates the correctness of theoretical analysis results in (10). The counter-intuitive phenomenon that V_{PCC} decreases and Δsg increases as X_g increases actually results from the PCC voltage-based vector control [23]. If the GCI is under grid voltage-based vector control, the increment of X_g should lead to an increment of V_{PCC}. Note that the simulation results are not accurate when L_g is larger than 8 mH, since the system becomes unstable under weak grid condition. It means that steady-state point acquirement method based on power flow simulation is not applicable when the grid is weak.

Fig. 7 shows the simulation results of V_{PCC} and Δsg with $I_{g,d}^{ref}$ varying from 100 A to 800 A with step size 100 A when $R_g = 0$, $L_g = 2$ mH and $I_{g,q}^{ref} = 0$. In addition, the theoretical V_{PCC} and Δsg can be calculated by (10), i.e., $V_{PCC} = \sqrt{V_g^2 - (X_g I_{g,d}^{ref})^2} = \sqrt{469.49^2 - (0.628 I_{g,d}^{ref})^2}$ and $\Delta sg = \cos^{-1} \frac{\sqrt{469.49^2 - (0.628 I_{g,d}^{ref})^2}}{469.49}$, which are also plotted in Figs. 7(a), (b). It can be seen that the simulation results highly agree with the theoretical analysis results, which validates the correctness of theoretical analysis results in (10). It can also be seen that V_{PCC} decreases and Δsg increases as $I_{g,d}^{ref}$ increases. Similar with Fig. 6, the counter-intuitive phenomenon also results from the PCC voltage-based vector control. In addition, high active power level makes the system unstable, and simulation results are not accurate anymore.

Fig. 8 shows the simulation results of V_{PCC} with $I_{g,q}^{ref}$ varying from -400 A to 400 A when $R_g = 0$, $L_g = 2$ mH and $I_{g,d}^{ref} = 100$ A. In addition, the theoretical V_{PCC} can be calculated by (10), i.e., $V_{PCC} = \sqrt{V_g^2 - (X_g I_{g,d}^{ref})^2} = \sqrt{469.49^2 - (31400 L_g)^2}$, which also plotted in Figs. 8(a), (b). It can be seen that the simulation results highly agree with the theoretical analysis results, which validates the correctness of theoretical analysis results in (10). Note that when under current control mode, reactive power injection does not influence system stability, whereas the system stability will be influenced under power control mode [14].

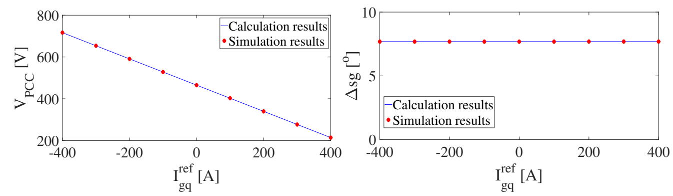

(a) (b)

Fig. 8. Impacts of $I_{g,q}^{ref}$ on V_{PCC} and Δsg. (a) Impact of $I_{g,q}^{ref}$ on V_{PCC}. (b) Impact of $I_{g,q}^{ref}$ on Δsg.

2) Impact of X_g on $\mathbf{Z_{s\_dq}}$: Since Z_{qq} of the dq impedance model plays an important role in low-frequency stability assessment, Fig. 9 shows the Bode diagram of Z_{qq} component with L_g varying from 0 mH to 14 mH with step size 2 mH when $R_g = 0$, $I_{g,d}^{ref} = 100$ A and $I_{g,q}^{ref} = 0$. It can be seen that low-frequency impedance characteristic is influenced by grid impedance. Specifically, Fig. 9(b) shows that phase angle in low-frequency range increases as L_g increases.

B. Influence of GCI Part on the Modified DQ Impedance Model of Grid Part

Fig. 10 shows the calculation results of $\frac{1}{A}$ and $\frac{1}{B}$ with L_g varying from 0 to 20 mH with step size 1 mH when $R_g = 0$, $I_{g,d}^{ref} = 100$ A and $I_{g,q}^{ref} = 0$ using (20), i.e., $\frac{1}{A} = \frac{1}{\sqrt{(\frac{469.49}{31400 L_g})^2 - 1}}$ and $\frac{1}{B} = \frac{1}{\sqrt{(\frac{469.49}{\sqrt{469.49^2 - (31400 L_g)^2}})^2 - 1}}$. It can be seen that $\frac{1}{A}$ and $\frac{1}{B}$ are zero when L_g exceeds a certain threshold value. We can derive from (16) and (23) that under

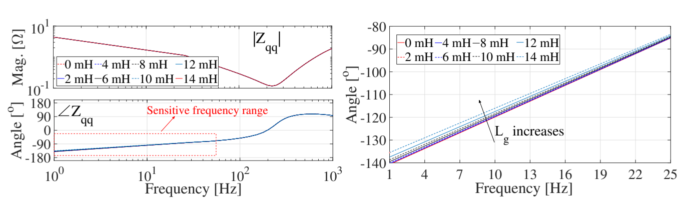

(a) (b)

Fig. 9. Impacts of L_g on Z_{qq} of the dq impedance model of GCI part. (a) Impact of L_g on Z_{qq}. (b) Zoomed figure of phase angle diagram.

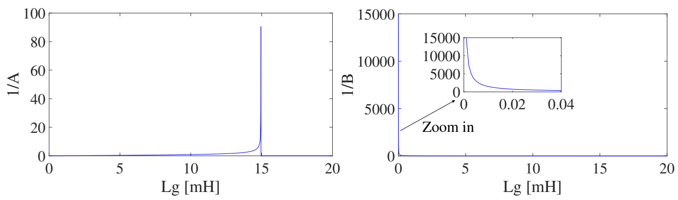

(a) (b)

Fig. 10. Impacts of X_g on $\frac{1}{A}$ and $\frac{1}{B}$. (a) Impact of X_g on $\frac{1}{A}$. (b) Impact of X_g on $\frac{1}{B}$.

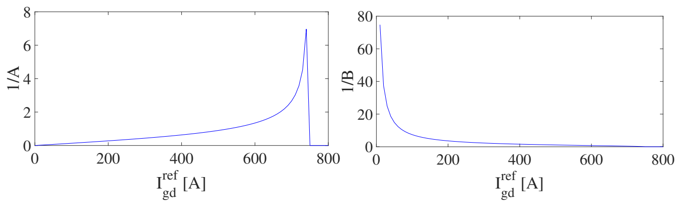

(a) (b)

Fig. 11. Impacts of $I_{g,d}^{ref}$ on $\frac{1}{A}$ and $\frac{1}{B}$. (a) Impact of $I_{g,d}^{ref}$ on $\frac{1}{A}$. (b) Impact of $I_{g,d}^{ref}$ on $\frac{1}{B}$.

weak grid condition, the modified dq impedance model of the grid part can be simplified as the conventional dq impedance model.

Fig. 11 shows the calculation results of $\frac{1}{A}$ and $\frac{1}{B}$ with $I_{g,d}^{ref}$ varying from 0 to 800 A when $R_g = 0$, $L_g = 2$ mH and $I_{g,q}^{ref} = 0$ using (20), i.e., $\frac{1}{A} = \frac{1}{\sqrt{(\frac{469.49}{0.628 I_{g,d}^{ref}})^2 - 1}}$ and $\frac{1}{B} = \frac{1}{\sqrt{(\frac{469.49}{\sqrt{469.49^2 - (0.628 I_{g,d}^{ref})^2}})^2 - 1}}$. It can be seen that $\frac{1}{A}$ increases as $I_{g,d}^{ref}$ increases from 0 A to 750 A, and decreases as $I_{g,d}^{ref}$ increases from 750 A to 800 A. In addition, $\frac{1}{B}$ decreases to zero quickly as $I_{g,d}^{ref}$ increases. No that both $\frac{1}{A}$ and $\frac{1}{B}$ are zero when enough high active current is injected.

Similarly, Fig. 12 shows the calculation results of $\frac{1}{A}$ and $\frac{1}{B}$ with $I_{g,q}^{ref}$ varying from -400 A to 400 A when $R_g = 0$, $L_g = 2$ mH and $I_{g,d}^{ref} = 100$ A using (20), i.e., $\frac{1}{A} = \frac{1}{\sqrt{(\frac{469.49}{62.8})^2 - 1}}$ and $\frac{1}{B} = \frac{1}{\sqrt{(\frac{469.49}{\sqrt{469.49^2 - (62.8)^2}})^2 - 1}}$. It can be seen that both $\frac{1}{A}$ and $\frac{1}{B}$ are constant.

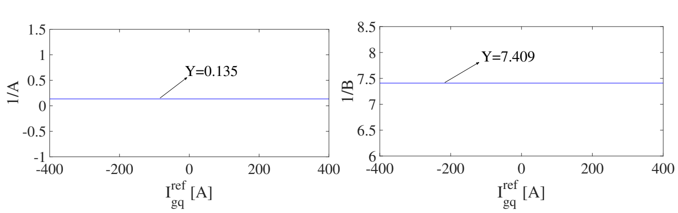

(a) (b)

Fig. 12. Impacts of $I_{g,q}^{ref}$ on $\frac{1}{A}$ and $\frac{1}{B}$. (a) Impact of $I_{g,q}^{ref}$ on $\frac{1}{A}$. (b) Impact of $I_{g,q}^{ref}$ on $\frac{1}{B}$.

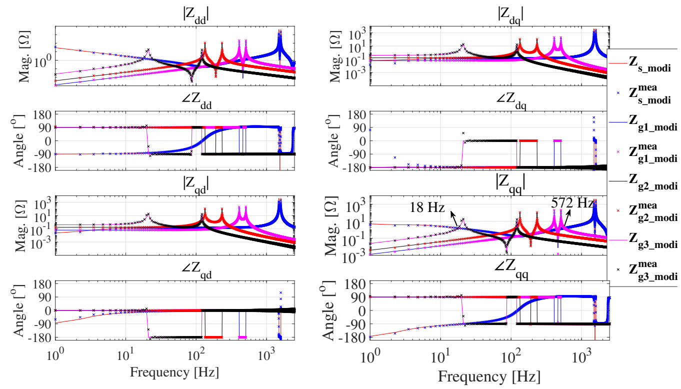

Fig. 13. Bode diagrams of dq impedance frequency responses of GCI part and grid part obtained by proposed dq impedance models and frequency scanning.

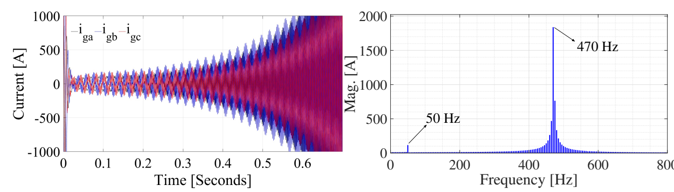

(a) (b)

Fig. 14. Time-domain simulation results and FFT of grid current when $L_g = 2$ mH and $C_g = 60\mu$F. (a) Time-domain simulation results. (b) FFT result.

C. Verification of Effectiveness of the Modified DQ Impedance Model of the GCI-Grid Coupling System for Stability Analysis

Fig. 13 shows the Bode plots of the theoretically-derived dq impedance models of GCI part using the proposed model $\mathbf{Z_{s\_modi}}$ and measured impedance frequency responses $\mathbf{Z_{s\_modi}^{mea}}$. It can be seen that the $\mathbf{Z_{s\_modi}^{mea}}$ highly agrees with $\mathbf{Z_{s\_modi}}$. In addition, Bode diagrams of the theoretically-derived dq impedance models of grid part using the proposed model and measured impedance frequency responses of three grid conditions, i.e., case 1: $L_g = 2$ mH and $C_g = 60\mu$F, case 2: $L_g = 5$ mH and $C_g = 150\mu$F, and case 3: $L_g = 13$ mH and $C_g = 390\mu$F, are also plotted in Fig. 13. It can be seen that high-frequency oscillation happens at 472 Hz (572-100=472 Hz) under case 1. System is stable under case 2. Low-frequency oscillation happens at 68 Hz and 32 Hz (50+18=68 Hz and 50-18=32 Hz) under case 1.

Figs. 14-16 show time-domain simulation results of grid current and corresponding frequency spectrum under the three grid conditions, which agree with the Bode plots in Fig. 13. The simulation results verifies the effectiveness of the proposed dq impedance modelling method of the GCI-grid coupling system for stability analysis.

V. Conclusion

This paper presents novel dq impedance models of GCI part and grid part for stability analysis. As for the dq impedance model of GCI part, steady-state operation point, e.g., duty cycle, dq axles currents and terminal voltage is not required. Instead, grid parameters, i.e., grid impedance and grid voltage

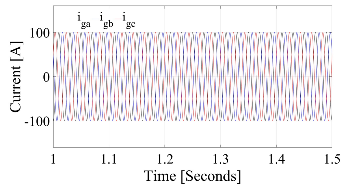

Fig. 15. Time-domain simulation results of grid current when $L_g = 5$ mH and $C_g = 150\mu$F.

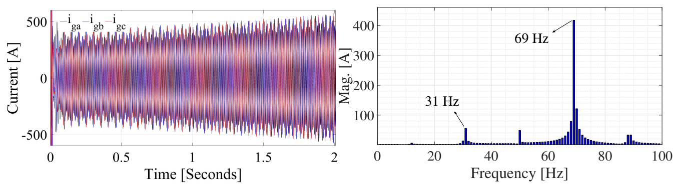

(a) (b)

Fig. 16. Time-domain simulation results and FFT of grid current when $L_g =$ 13 mH and $C_g = 390\mu$F. (a) Time-domain simulation results. (b) FFT result.

are included in the modified dq impedance model of the GCI part. The proposed dq impedance modelling method of GCI need not run power flow to obtain steady-state operating point, which may be not practical for unstable system. As for the impedance model of grid part, conventional dq impedance model is modified to consider the effects of dynamics of grid voltage and PLL. Measured dq impedance models using frequency scanning method highly agree with the modified dq impedance models of GCI part and grid part, indicating the correctness of the proposed impedance modelling method. In addition, system stability characteristics can be predicted by the modified system dq impedance model. The proposed dq impedance model of the whole system may provide more insights to reveal the oscillation mechanism than the conventional dq impedance model where GCI part and grid part are modelled independently.

References

[1] F. Blaabjerg, Z. Chen, and S. B. Kjaer, "Power electronics as efficient interface in dispersed power generation systems," *IEEE Trans. Power Electron.*, vol. 19, no. 5, pp. 1184–1194, Sep. 2004.

[2] D. Dong, B. Wen, D. Boroyevich, P. Mattavelli, and Y. Xue, "Analysis of phase-locked loop low-frequency stability in three-phase grid-connected power converters considering impedance interactions," *IEEE Trans. Ind. Electron.*, vol. 62, no. 1, pp. 310–321, Jan. 2015.

[3] B. Wen, D. Boroyevich, R. Burgos, P. Mattavelli, and Z. Shen, "Analysis of DQ small-signal impedance of grid-tied inverters," *IEEE Trans. Power Electron.*, vol. 31, no. 1, pp. 675–687, Jan. 2016.

[4] X. Wang and F. Blaabjerg, "Harmonic stability in power electronic based power systems: concept, modeling, and analysis," *IEEE Trans. Smart Grid*, vol. 10, no. 3, pp. 2858–2870, May 2019.

[5] J. Sun, "Impedance-based stability criterion for grid-connected inverters," *IEEE Trans. Power Electron.*, vol. 26, no. 11, pp. 3075–3078, Nov. 2011.

[6] W. Zhou, Y. Wang, and Z. Chen, "Impedance-decoupled modelling method of multi-port transmission network in inverter-fed power plant," *IEEE Trans. Ind. Appl.*, Early Access.

[7] S. Shah and L. Parsa, "Impedance modeling of three-phase voltage source converters in DQ, sequence, and phasor domains," *IEEE Trans. Energy Convers.*, vol. 32, no. 3, pp. 1139–1150, Sep. 2017.

[8] W. Zhou, Y. Wang, and Z. Chen, "Decoupled multi-port impedance modelling method of transmission network in inverter-fed power plant," in *Proc. IEEE 2018 International Conference on Smart Grid (icSmartGrid)*, pp. 129–135.

[9] C. Yoon, H. Bai, R. N. Beres, X. Wang, C. L. Bak, and F. Blaabjerg, "Harmonic stability assessment for multiparalleled, grid-connected inverters," *IEEE Trans. Sustain. Energy*, vol. 7, no. 4, pp. 1388–1397, Oct. 2016.

[10] W. Zhou, Y. Wang, and Z. Chen, "A gray-box parameters identification method of voltage source converter using vector fitting algorithm," in *Proc. IEEE 2019 ICPE-ECCE Asia)*, pp. 2948–2955.

[11] M. Cespedes and J. Sun, "Impedance modeling and analysis of grid-connected voltage-source converters," *IEEE Trans. on Power Electron.*, vol. 29, no. 3, pp. 1254–1261, Mar. 2014.

[12] W. Cao, Y. Ma, and F. Wang, "Sequence-impedance-based harmonic stability analysis and controller parameter design of three-phase inverter-based multibus AC power systems," *IEEE Trans. Power Electron.*, vol. 32, no. 10, pp. 7674–7693, Oct. 2016.

[13] W. Cao, Y. Ma, L. Yang, F. Wang, and L. M. Tolbert, "D–Q impedance based stability analysis and parameter design of three-phase inverter-based AC power systems," *IEEE Trans. Ind. Electron.*, vol. 64, no. 7, pp. 6017–6028, Jul. 2017.

[14] W. Zhou, Y. Wang, D. Liu, and Z. Chen, "Optimization of active and reactive power dispatch among multi-paralleled grid-connected inverters considering low-frequency stability," in *Proc. IEEE 2019 45th Annual Conference of the IEEE Industrial Electronics Society (IES)*, pp. 6024–6031.

[15] A. Rygg, M. Molinas, C. Zhang, and X. Cai, "A modified sequence-domain impedance definition and its equivalence to the dq-domain impedance definition for the stability analysis of AC power electronic systems," *IEEE J. Emerg. Sel. Topics Power Electron.*, vol. 4, no. 4, pp. 1383–1396, Dec. 2016.

[16] C. Zhang, X. Cai, A. Rygg, and M. Molinas, "Sequence domain SISO equivalent models of a grid-tied voltage source converter system for small-signal stability analysis," *IEEE Trans. Energy Convers.*, vol. 33, no. 2, pp. 741–749, Jun. 2017.

[17] A. Rygg, M. Molinas, C. Zhang, and X. Cai, "On the equivalence and impact on stability of impedance modeling of power electronic converters in different domains," *IEEE J. Emerg. Sel. Topics Power Electron.*, vol. 5, no. 4, pp. 1444–1454, Dec. 2017.

[18] B. Wen, R. Burgos, D. Boroyevich, P. Mattavelli, and Z. Shen, "AC stability analysis and dq frame impedance specifications in power-electronics-based distributed power systems," *IEEE J. Emerg. Sel. Topics Power Electron.*, vol. 5, no. 4, pp. 1455–1465, Dec. 2017.

[19] A. Rygg, M. Molinas, E. Unamuno, C. Zhang, and X. Cai, "A simple method for shifting local dq impedance models to a global reference frame for stability analysis," *arXiv preprint arXiv:1706.08313*.

[20] L. Fan and Z. Miao, "An explanation of oscillations due to wind power plants weak grid interconnection," *IEEE Trans. Sustain. Energy*, vol. 9, no. 1, pp. 488–490, Jan. 2017.

[21] D. Yang, X. Wang, F. Liu, K. Xin, Y. Liu, and F. Blaabjerg, "Adaptive reactive power control of PV power plants for improved power transfer capability under ultra-weak grid conditions," *IEEE Trans. Smart Grid*, vol. 10, no. 2, pp. 853–864, Mar. 2019.

[22] L. Fan, "Modeling type-4 wind in weak grids," *IEEE Trans. Sustain. Energy*, vol. 10, no. 2, pp. 853–864, Apr. 2019.

[23] Y. Li, L. Fan, and Z. Miao, "Stability control for wind in weak grids," *IEEE Trans. Sustain. Energy*, vol. 10, no. 4, pp. 2094–2103, Oct. 2019.

[24] J. Liu, X. Du, Y. Shi, and H.-M. Tai, "Grid-connected inverter impedance estimation considering grid impedance and frequency coupling in the stationary frame," in *Proc. IEEE 2019 11th Energy Conversion Congress and Exposition (ECCE)*, pp. 6214–6218.

[25] Q. Qian, N. Zhong, S. Xie, J. Xu, and B. Zhang, "Impact of the grid impedance on the single-phase grid-connected inverter output impedance concerning the frequency-coupling effect of the PLL," in *Proc. IEEE 2019 45th Annual Conference of the IEEE Industrial Electronics Society (IES)*, pp. 2225–2230.